ROYAL SOCIETY
OF CHEMISTRY

PAPER

Check for updates

Methanol-induced fast CsBr release results in phase-pure CsPbBr₃ perovskite nanoplatelets

Xin Liu,†[a] Zhao Luo,†[a] Wenxu Yin,[a] Aleksandr P. Litvin, [b] Alexander V. Baranov, [b] Jiaqi Zhang,[a] Wenyan Liu,[c] Xiaoyu Zhang [*a] and Weitao Zheng [*a]

Formation of a non-emissive wide bandgap $CsPb_2Br_5$ component often accompanies the synthesis of $CsPbBr_3$ perovskites, introducing undesired energy states and impeding the charge transport. Here, we demonstrate that a small amount of a methanol additive can promote the CsBr release rate, facilitating $CsPbBr_3$ formation and suppressing $CsPb_2Br_5$ formation. Some of the methanol ionizes into CH_5O^+ and CH_3O^-, which act as surface ligands and change the crystallization environment, inducing shape evolution from spherical nanocrystals to rectangular nanoplatelets (NPLs), leading to monodispersed and phase-pure 8 unit-cell-thick $CsPbBr_3$ NPLs. Meanwhile, nonradiative recombination processes are inhibited as a result of NPL surface passivation. Bright $CsPbBr_3$ NPLs with a photoluminescence quantum yield reaching 90% were employed as emitters for electroluminescent light-emitting devices.

Introduction

Metal halide semiconductors with a perovskite crystal structure are famous for their excellent electrical and optical properties.[1-5] Showing high photoluminescence (PL) quantum yields (QYs),[6,7] an optimal range of band gap energy values and high defect tolerance,[8-11] the perovskite nanomaterials hold great promise for solar cell,[12] photodetector,[13] laser,[14,15] light-emitting diode (LED) and display applications.[16-30] Being free from the organic component, the all inorganic $CsPbX_3$ (X^- stands for halide ions) perovskites are compositionally stable up to their melting points which are in excess of 460 °C,[31] and thus have attracted enormous interest.

Different from traditional covalent semiconductor nanocrystals (NCs), whose synthesis requires a high temperature to decompose the precursor,[32-35] perovskite NCs can be synthesized at room temperature *via* a ligand assisted reprecipitation (LARP) approach,[36,37] which is due to its ionic nature.[38,39] By controlling the surface ligands, reaction temperature and additives, several shape variations of perovskite nanomaterials have been achieved, including NCs, nanorods, nanowires, and nanoplatelets (NPLs).[40-48] However, taking $CsPbBr_3$ as an example, even though the Cs : Pb : Br ratio is set precisely to 1 : 1 : 3 in the precursor, the final products are always accompanied by $CsPb_2Br_5$ impurities, which are known as nonemissive wide bandgap components.[49-52] These impurities introduce undesired energy states and act as charge blockers, decreasing the charge mobility.[53] We propose the nonuniform precursor release rate to be the main cause of the formation of $CsPb_2Br_5$ byproducts, and this general idea is demonstrated here. The CsBr release rate was controlled by introducing trace amounts of methanol into the LARP approach. With 600 μL of the methanol additive, the byproduct $CsPb_2Br_5$ disappeared and monodispersed 8 unit-cell-thick $CsPbBr_3$ NPLs were obtained. With the help of oleic acid (OA) and oleylamine (OLA), the methanol was partly ionized into CH_5O^+ and CH_3O^-, which partially replaced OA and/or OLA surface ligands, inducing the formation of rectangular NPLs. Bright $CsPbBr_3$ NPLs with a photoluminescence quantum yield (PL QY) reaching 90% were employed as emitters for electroluminescent light-emitting devices, with a peak luminance of 8347 cd m^{-2} and current efficiency of 13.2 cd A^{-1}.

Results and discussion

The synthesis of $CsPbBr_3$ NPLs can be divided into three steps, as shown in Scheme 1. First, the precursor solution was prepared by mixing 0.4 mmol CsBr, 0.4 mmol $PbBr_2$, 0.5 mL OLA, and 1 mL OA in 10 mL DMF (dimethylformamide, the "good solvent"). Then, x μL ($0 \leq x \leq 800$) methanol was added into 10 mL toluene, namely the "bad solvent". Finally, 1 mL of the precursor solution was injected into 10 mL of the "bad solvent" to trigger supersaturation. The UV-vis absorption and PL spectra of the as-synthesized $CsPbBr_3$ are shown in Fig. 1a and b, respectively. The absorption spectra gradually red-shift as the amount of methanol added increases from 0 to 800 μL,

[a]Key Laboratory of Automobile Materials, Ministry of Education, College of Materials Science and Engineering, Jilin University, Changchun, 130012, P. R. China. E-mail: zhangxiaoyu@jlu.edu.cn; wtzheng@jlu.edu.cn

[b]Center of Information Optical Technology, ITMO University, 49 Kronverksky Pr., St. Petersburg 197101, Russia

[c]College of Materials Science & Engineering, Beihua University, Jilin, 132013, P. R. China

† X. Liu and Z. Luo contributed equally to this work.
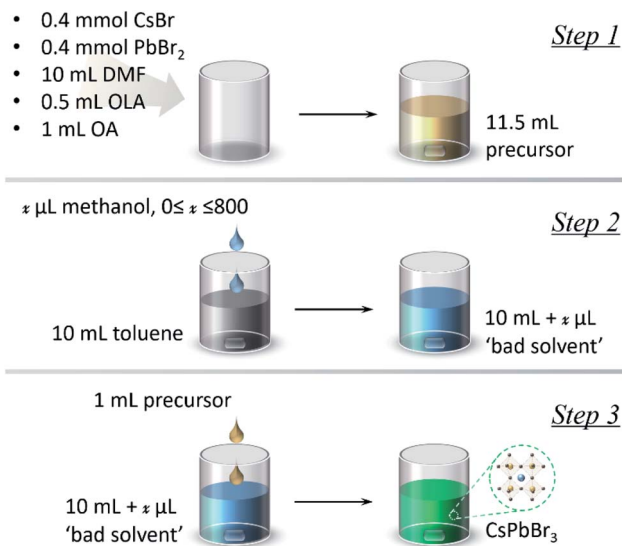
Scheme 1 Schematic representation of the synthesis of the CsPbBr$_3$ NPLs by a modified LARP approach.
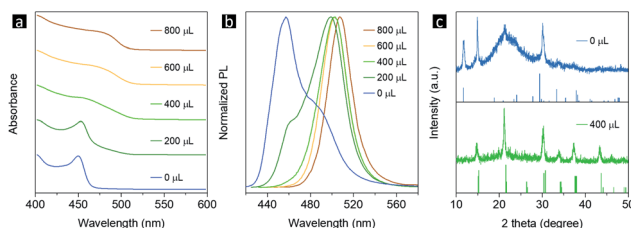

Fig. 1 (a) UV-vis absorption spectra, (b) PL spectra, and (c) XRD patterns of CsPbBr$_3$ NCs synthesized using the LARP method; the numbers in the frame are the volume of methanol added into toluene. The line XRD pattern in blue shows peaks for the CsPb$_2$Br$_5$ phase, and the one in green shows peaks for the orthorhombic CsPbBr$_3$ phase.

and the corresponding PL peaks red-shift from 460 to 507 nm. There are additional shoulders in the PL spectra for samples with 0 and 200 μL methanol, indicating that the finally products of these two samples contain several different fluorescence centers. When the amount of added methanol reaches 400 μL, the PL spectrum follows a Gaussian peak shape and the emission bandwidth decreases to 30 nm, which is consistent with typical CsPbBr$_3$ emission, demonstrating that a mono fluorescence center exists in the sample.[54] In addition, the absolute PL QY of CsPbBr$_3$ without methanol is 50%, while it increases to 90% when 600 μL methanol is introduced. The above optical characterization results demonstrate that a suitable amount of the methanol additive can help to purify the final product and improve the PL properties.

Determining the kind of impurities that have been inhibited from appearing *via* introducing methanol is the basis for understanding the mechanism of the methanol assisted LARP approach. X-Ray diffraction (XRD) characterization was used to address this issue. Since the PL started follow the characteristics of typical CsPbBr$_3$ emission when the amount of methanol additive used was increased to 400 μL, this sample at the

turning point was chosen to be compared with the products obtained without using methanol. As shown in Fig. 1c, an impurity CsPb$_2$Br$_5$ phase can be recognized besides the desired CsPbBr$_3$ component in the product without methanol, while this impurity disappears and pure CsPbBr$_3$ can be obtained in the sample after 400 μL methanol is added. The chemical reactions involved are given as follows:

$$Cs^+ + 2Pb^{2+} + 5Br^- \rightarrow CsPb_2Br_5 \qquad (1)$$

$$Cs^+ + Pb^{2+} + 3Br^- \rightarrow CsPbBr_3 \qquad (2)$$

As shown, when the elemental ratio of Cs : Pb : Br is equal to 1 : 2 : 5, the final product is CsPb$_2$Br$_5$, while when the elemental ratio of Cs : Pb : Br is equal to 2 : 2 : 6, the final product changes to CsPbBr$_3$. Clearly, more Cs$^+$ and Br$^-$ ions are needed to form CsPbBr$_3$ instead of CsPb$_2$Br$_5$. CsBr easily dissolves in methanol to form a high concentration solution of 15 mg mL^{-1}, and PbBr$_2$ is insoluble in methanol, implying that methanol mainly influences the release of Cs$^+$ and Br$^-$.[55] On comparing this with our experimental results, it can be seen that without methanol there will be excessive Pb^{2+} ions which leads to CsPb$_2$Br$_5$ and CsPbBr$_3$ NCs with Pb-rich surfaces, and after introducing the methanol additive there will be more Cs$^+$ and Br$^-$ ions which favours the formation of CsPbBr$_3$ NCs with more Br$^-$ ions on the surfaces. Since lead rich surfaces have lots of electron traps while PbBr-terminated surfaces are known for fewer surface traps,[25] we can deduce that the PL QY increase of NCs with the methanol additive benefits from the passivation of Pb-rich surfaces. A faster CsBr release rate induces the formation of CsPbBr$_3$, while more Br$^-$ ions passivate uncoordinated lead atoms, together inducing the formation of phase-pure and bright CsPbBr$_3$ perovskites.

However, CsPb$_2$Br$_5$ is known as non-emissive perovskite[50] and will not change the PL of CsPbBr$_3$. There must be other reasons causing the PL peak broadening with additional emission shoulders. Besides impurities, size and shape variation could also result in different emission colors,[56,57] which is due to changes in the quantum confinement effect within CsPbBr$_3$ and thus the bandgaps. Transmission electron microscopy (TEM) measurements were performed to confirm whether there is a size and/or shape variation. Fig. 2a and b show TEM images from different regions of the same sample without the methanol additive, revealing that this sample is a mixture of ∼2 nm spherical NCs (Fig. 2a), ∼6 nm spherical NCs and irregularly shaped NPLs (Fig. 2b). The height of the spherical NCs was determined to be app. 2 nm by atomic force microscopy (AFM, Fig. 3a), which is consistent with the TEM results. Following the size-dependent PL behavior, we can easily match the PL components with the obtained NCs or NPLs. As shown in Fig. 4, the PL spectrum of the sample without the methanol additive was fitted using Gaussian fitting. The emission peak at 455 nm originates from the ∼2 nm NCs, the emission peaks at 480 and 500 nm originate from the ∼6 nm NCs and irregularly shaped NPLs, and the emission peak at 520 nm is trap state related PL. For TEM characterization, the contrast in the image can reflect the thickness of the crystals: high contrast means thick crystals
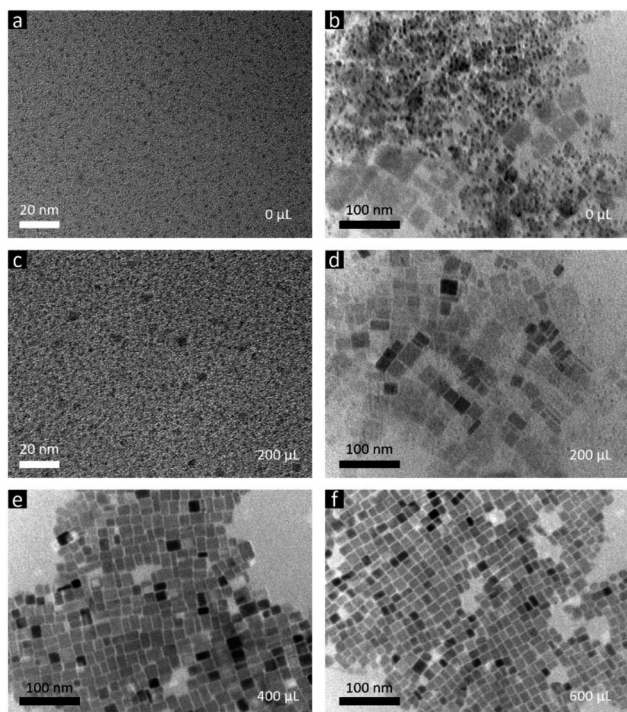
Fig. 2 TEM images of the final products from the LARP approach using different amounts of methanol: (a) and (b) 0 μL, (c) and (d) 200 μL, (e) 400 μL, and (f) 600 μL.

while low contrast stands for thin nanoplatelets. As shown in Fig. 2d, for the samples with 200 μL methanol, the contrast of most crystals is very low, indicating that they are thin nanoplatelets benefiting from the quantum confinement effect and exhibiting PL peaks at wavelengths less than 525 nm (corresponding to the bulk bandgap). The few high contrast crystals may contribute to the long tail of the PL spectrum at longer wavelengths. Thus, based on the PL spectrum (Fig. 1b) and the TEM images (Fig. 2c and d) of the sample using 200 μL of the methanol additive, we can observe a similar relationship between the PL components and the observed NCs and NPLs. The wide size and shape distribution is determined to be the main cause of these wide and asymmetrical PL spectra.

When the amount of the methanol additive reached 400 μL, the spherical NCs disappeared and only rectangular NPLs with an edge length varying from 12 to 26 nm were observed (Fig. 2e

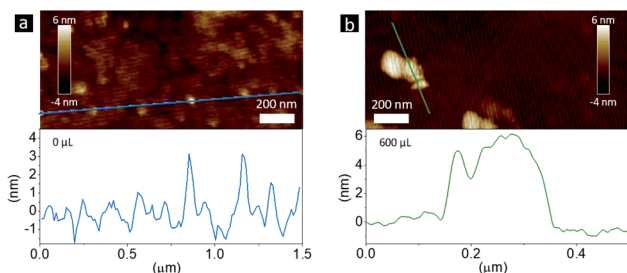
Fig. 3 AFM images and the corresponding height analysis of samples (a) without and (b) with 600 μL of the methanol additive.
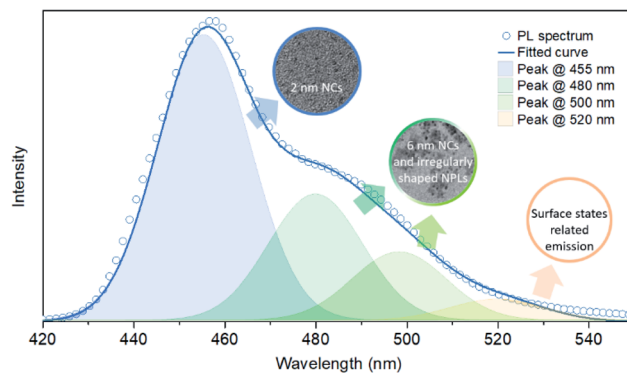

Fig. 4 Gaussian fitting of the PL spectrum of the sample without the methanol additive, and the relationship between these PL components and the obtained NCs and NPLs.

and 5). Increasing the amount of methanol to 600 μL narrowed the NPL edge length distribution to 12 to 19 nm (Fig. 2f and 5). The Bohr exciton diameter of $CsPbBr_3$ has been determined to be 7 nm,[56] which is much smaller than the NPL edge length (18.9 ± 4.7 and 15.7 ± 2.1 nm for samples using 400 and 600 μL methanol, respectively, Fig. 5). The emission maximum of bulk $CsPbBr_3$ is located at 525 nm,[58] which is red-shifted by 23 nm relative to the samples using 400 and 600 μL methanol (both at 502 nm), demonstrating a strong quantum confinement effect. Thus, the thickness of these NPLs should be less than the Bohr exciton diameter of 7 nm. That's the reason for naming them NPLs. The PL peaks of 400 and 600 μL NPLs coincide, representing similar quantum confinement effects and thus similar thicknesses. The thickness (height) of the 600 μL sample was determined to be app. 5 nm by AFM (Fig. 3b), corresponding to 8 unit-cell-thick NPLs.

The possible growth process of $CsPbBr_3$ NPLs with or without the presence of traces of methanol is shown schematically in Scheme 2. Without methanol, ultrasmall 2 nm spherical NCs form first. Some of these ultrasmall particles aggregate together to form 6 nm spherical NCs and irregular NPLs due to the large surface to volume ratio of the 2 nm NCs and insufficient number of ligands, while the others interact with Pb^{2+} and
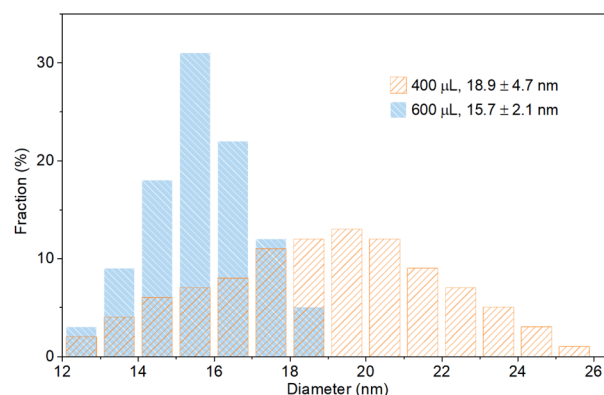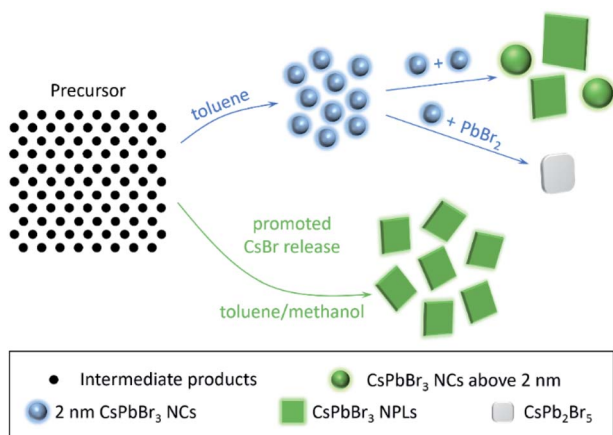

Fig. 5 Edge length distribution histograms of $CsPbBr_3$ NPLs synthesized with 400 and 600 μL of the methanol additive.

Scheme 2 Schematic representation of the LARP approach carried out with or without the presence of traces of methanol.

Br^- ions to form $CsPb_2Br_5$ due to the lack of Cs^+ ions. After introducing methanol, the Cs^+ and Br^- release rate is promoted. More Cs^+ and Br^- ions induce the formation of $CsPbBr_3$, while more Br^- ions passivate uncoordinated lead atoms, together inducing the formation of phase-pure and bright $CsPbBr_3$ NPLs. The absolute PL QY and the PL peak's full-width at half-maximum (FWHM) as functions of the methanol volume are summarized in Fig. 6a. With the increasing amount of methanol from 0 to 600 μL, the FWHM decreases from 40 to 27 nm, and the PL QY increases from 50% to 90%, which is due to the increased number of Br^- ions passivating the NC surfaces during crystallization. The PL QY decreases to 75% when the methanol additive is increased to 800 μL, due to the decomposition of $CsPbBr_3$ perovskites by excessive methanol. The brightest sample with 600 μL of the methanol additive was chosen to investigate the electron–hole recombination mechanisms. The time-resolved PL decay (TRPL) of the as-prepared $CsPbBr_3$ without and with 600 μL methanol is presented in Fig. 6b. The decay fitting results are listed in Fig. 6c. The short lifetime component (10.2 and 18.0 ns for samples with 0 and
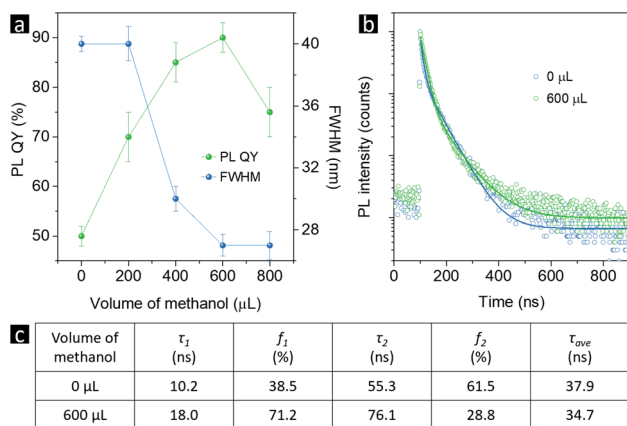
600 μL methanol, respectively) originates from the exciton radiative recombination, whereas the long-lived component (55.3 and 76.1 ns for samples with 0 and 600 μL methanol, respectively) is consistent with delayed PL caused by surface traps. Clearly, the relative ratio of amplitude (f_1) of τ_1 to that (f_2) of τ_2 increased obviously with the methanol additive (more Br^- ions during crystallization), indicating that some of the surface traps have been modified. As for the shape evolution from spherical NCs to rectangular NPLs after introducing methanol, it is supposed to be related to the changed crystallization environment. Typically, the high-energy facets grow faster than the low-energy facets during perovskite crystallization, and the surface energy of certain facets can be lowered by binding with surface ligands. Indeed, it has been well documented in the literature that NPLs could be obtained *via* introducing short ligands, like pyridine, octanoic acid and octylamine.[43,44,59] In our case, with the help of OA^- and OLA^+, some of the methanol can ionize into CH_5O^+ and CH_3O^-, which act as surface ligands and change the crystallization environment,[58,60] inducing shape evolution from spherical nanocrystals to rectangular NPLs.

The $CsPbBr_3$ NPLs with the highest PL QY were chosen as emitters for electroluminescence (EL) light-emitting diodes (LEDs). Ultraviolet photoelectron spectroscopy (UPS) measurements (Fig. 7a) were performed on $CsPbBr_3$ NPL films in order to map the valence band maximum (VBM) and the conduction band minimum (CBM). The Tauc plot of a $CsPbBr_3$ NPL film on a quartz substrate (Fig. 7b) exhibits a bandgap of 2.37 eV. Thus, the VBM and CBM values for $CsPbBr_3$ NPLs are determined to be −5.80 and −3.43 eV, respectively. A schematic of the $CsPbBr_3$ NPL LED device structure used in this study is shown in Fig. 8a. The device energy band diagram for all functional layers is given in Fig. 8b. The LED comprised a layer of $CsPbBr_3$ NPLs deposited on top of an ITO/ZnO substrate with a top 4,4,4″-tris(carbazol-9-yl)triphenylamine (TCTA)/MoO_3/Au electrode. The wide bandgap ZnO is famous for its high electron mobility, excellent optical transparency and deep lying VBM, and thus was chosen as the electron transport layer and the hole blocking layer.[61] TCTA has a HOMO (highest occupied molecular orbital) close to the VBM of $CsPbBr_3$ NPLs, and a low lying LUMO (lowest unoccupied molecular orbital) to block the electrons, and thus was chosen as the hole transport material.[62] A peak luminance of 8347 cd m^{-2} (Fig. 8c), a peak external quantum efficiency (EQE) of 4.2%, a peak current efficiency (CE) of 13.2 cd A^{-1}, and a peak power efficiency (LE) of 12.3 lm W^{-1} were

Fig. 6 (a) PL QY and FWHM values as functions of methanol volume. (b) TRPL curves and (c) the corresponding fitting results of samples without and with 600 μL of the methanol additive.

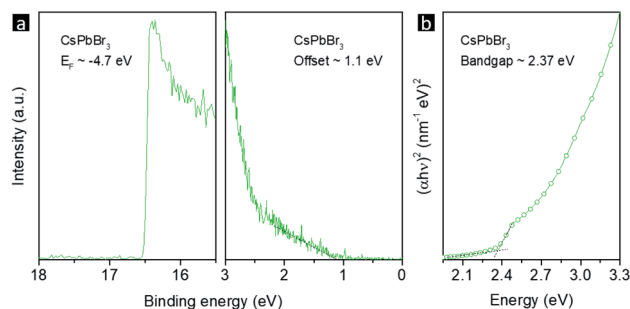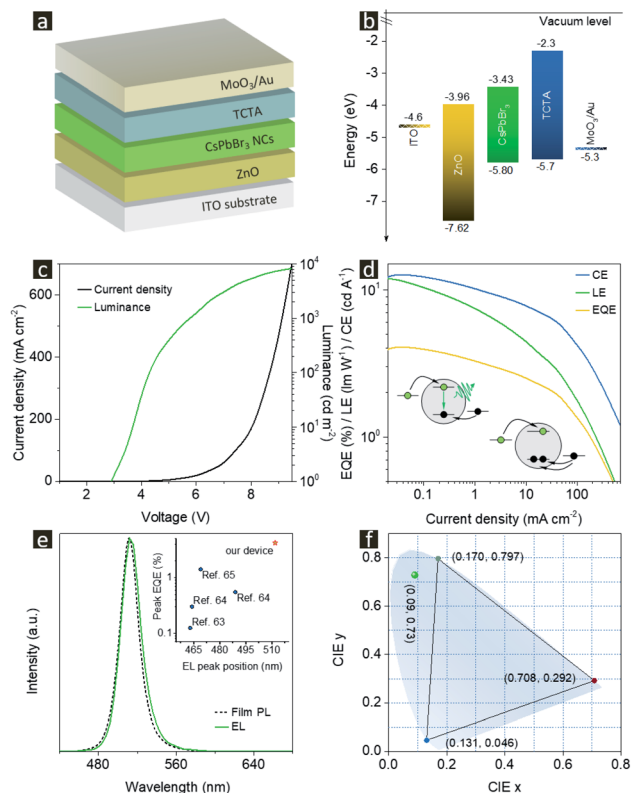| Volume of methanol	τ_1 (ns)	f_1 (%)	τ_2 (ns)	f_2 (%)	τ_{ave} (ns)
0 μL	10.2	38.5	55.3	61.5	37.9
600 μL	18.0	71.2	76.1	28.8	34.7

Fig. 7 (a) UPS spectra and (b) Tauc plots of $CsPbBr_3$ NPLs.

Fig. 8 (a) Schematic device architecture of the $CsPbBr_3$ NPL LED. (b) Energy diagram for all the functional layers employed in the optimized device. (c) Current density–voltage–luminance curves. (d) CE, LE, and EQE as a function of current density, with the inset showing the reasons for high efficiency "roll-off". (e) Device PL and EL spectra. The inset shows the comparison of device parameters between our device and reported $CsPbBr_3$ NPL LEDs. (f) The color coordinates of the $CsPbBr_3$ NPL LED on the CIE 1931 color space, together with the Rec. 2020 standard.

achieved (Fig. 8d). The EQE dropped to half of its initial value at 30 mA cm^{-2}, showing a high efficiency "roll-off". Unbalanced charge injection is the main cause for this. The electron injection barrier from ZnO to $CsPbBr_3$ NPLs is 0.53 eV, which is 0.43 eV larger than the hole injection barrier from TCTA to the emitters. At low current density, only limited amounts of charges can be transported to the emitters and the electrons would efficiently recombine with holes accompanied by emitting photons. At high current density, due to the smaller hole injection barrier, there will be more holes than electrons injected into the emissive layer, which leads to charged emitters that cannot emit photons any more. The schematic representation of these processes is shown in the inset of Fig. 8d. A bright EL solely from $CsPbBr_3$ NPLs peaking at 512 nm was observed, which matched the device PL except for a 2 nm increase in the FWHM (Fig. 8e). The CIE 1931 color coordinates of (0.09, 0.73) corresponding to the $CsPbBr_3$ NPL LED are shown in Fig. 8f, which is close to the Rec. 2020 standard. A summary of the emission peaks and EQE values of LEDs employing $CsPbBr_3$ NPLs is given in the inset of Fig. 8e. The emission peak of our NPL LED is located at the longest wavelength, which means narrower bandgaps and thus easier charge injection.

This may be the reason why our device EQE is higher than that of the others.[63–65]

Conclusions

In summary, we have explored the mechanism of the methanol-assisted LARP approach using lead bromide perovskite NCs as an example and have revealed how a suitable minor amount of a methanol additive leads to bright, monodispersed and phase-pure 8 unit-cell-thick $CsPbBr_3$ NPLs. It is the difference of the solubility in methanol between CsBr and $PbBr_2$ that determines the chemical reaction path: without methanol there is only a limited number of Cs^+ and Br^- ions participating in the reaction leading to formation of $CsPbBr_3$ accompanied by $CsPb_2Br_5$, while a suitable minor amount of the methanol additive promotes the CsBr release rate, resulting in phase-pure $CsPbBr_3$. The methanol additive can partly ionize into CH_5O^+ and CH_3O^-, which act as surface ligands partially replacing OLA^+ and OA^-, inducing shape evolution from spherical NCs to rectangular NPLs. The NPLs using 600 μL methanol exhibit a high PL QY of 90% and were employed as emitters resulting in bright LEDs with a peak brightness of 8347 cd m^{-2}. Our study demonstrated that a suitable polar solvent can activate the precursor leading to perovskite crystal growth control, providing new insights into phase- and shape-control over perovskite nanomaterials.

Experimental

Materials

Oleic acid (OA, 90%) was purchased from Alfa Aesar. Oleylamine (OLA, 80–90%), CsBr (99.9%), and $PbBr_2$ (99.0%) were purchased from Aladdin. Methanol ($\geq$99.9%) and dimethylformamide (DMF, 99.8%) were obtained from Sigma-Aldrich. TCTA (4,4,4″-tris(carbazol-9-yl)triphenylamine, 99%) was bought from jl-OLED.

Syntheses

As illustrated in Scheme 1, the synthesis of $CsPbBr_3$ NCs was carried out at room temperature by the LARP approach, through injection of 1 mL of the precursor mixture (which we denote using a generic term "precursor" hereafter) into a "bad solvent", toluene (10 mL) under vigorous stirring. The precursor was prepared by mixing CsBr (0.4 mmol), $PbBr_2$ (0.4 mmol), oleylamine (OLA, 0.5 mL), and oleic acid (OA, 1 mL) in a "good solvent", DMF (10 mL). Then, x μL ($0 \leq x \leq 800$) methanol was added into 10 mL toluene, namely the "bad solvent". In the end, 1 mL of the precursor solution was injected into 10 mL of the "bad solvent" to trigger supersaturation. Both the solvents, DMF and toluene, were dried to remove any remaining traces of water prior to use (DMF by adding $K_nNa_{12-n}[(AlO_2)_{12}(SiO_2)_{12}]$ and toluene via distillation).

LED fabrication

Patterned ITO-coated glass was carefully cleaned successively using soap, deionized water, ethanol, chloroform, acetone, and

isopropanol and was subjected to UV-ozone treatment for 15 min. A solution of ZnO NCs was spin-coated onto the ITO glass at 1000 rpm for 1 min and annealed in air at 150 °C for 10 min. The CsPbBr$_3$ NPL active layers were spin-cast at 1000 rpm for 1 min. 4,4′,4″-tris(carbazol-9-yl)-triphenylamine (TCTA), MoO$_3$, and Au films were sequentially deposited by thermal evaporation in a vacuum deposition chamber (1×10^{-7} Torr).

Characterization

Absorption and photoluminescence (PL) spectra were measured on a PerkinElmer Lambda 950 spectrometer and a Cary Eclipse spectrofluorimeter, respectively. Transmission electron microscopy (TEM) images were obtained on a FEI Tecnai F20 microscope. Powder XRD data were collected on a Bruker SMART-CCD diffractometer. The absolute PL QYs of the samples were measured on a fluorescence spectrometer (FLS920P, Edinburgh Instruments) equipped with an integrating sphere with its inner face coated with BENFLEC. Time-resolved PL measurements were performed with the time correlated single-photon counting (TCSPC) system of an FLS920P Edinburgh spectrometer. A 379 nm picosecond diode laser (EPL-375, repetition rate 5 MHz, 64.8 ps) was used to excite the samples. Ultraviolet photoelectron spectroscopy (UPS) spectra were collected on a PREVAC system. The electroluminescence spectra and the current density–luminance–voltage characteristics of LEDs were measured using a Keithley 2400 sourcemeter and a PR-670 SpectraScan Colorimeter.

Conflicts of interest

There are no conflicts to declare.

Acknowledgements

Notes and references

1 F. Huang, M. Li, P. Siffalovic, G. Cao and J. Tian, *Energy Environ. Sci.*, 2019, **12**, 518–549.

2 Q. Zhao, A. Hazarika, X. Chen, S. P. Harvey, B. W. Larson, G. R. Teeter, J. Liu, T. Song, C. Xiao, L. Shaw, M. Zhang, G. Li, M. C. Beard and J. M. Luther, *Nat. Commun.*, 2019, **10**, 2842.

3 H. Utzat, W. Sun, A. E. K. Kaplan, F. Krieg, M. Ginterseder, B. Spokoyny, N. D. Klein, K. E. Shulenberger, C. F. Perkinson, M. V. Kovalenko and M. G. Bawendi, *Science*, 2019, **363**, 1068–1072.

4 F. Wang, S. Bai, W. Tress, A. Hagfeldt and F. Gao, *npj Flexible Electron.*, 2018, **2**, 22.

5 X. Zhang, Q. Zeng, Y. Xiong, T. Ji, C. Wang, X. Shen, M. Lu, H. Wang, S. Wen, Y. Zhang, X. Yang, X. Ge, W. Zhang, A. P. Litvin, A. V. Baranov, D. Yao, H. Zhang, B. Yang, A. L. Rogach and W. Zheng, *Adv. Funct. Mater.*, 2020, **30**, 1910530.

6 F. Krieg, S. T. Ochsenbein, S. Yakunin, S. ten Brinck, P. Aellen, A. Süess, B. Clerc, D. Guggisberg, O. Nazarenko, Y. Shynkarenko, S. Kumar, C.-J. Shih, I. Infante and M. V. Kovalenko, *ACS Energy Lett.*, 2018, **3**, 641–646.

7 D. Yang, X. Li, W. Zhou, S. Zhang, C. Meng, Y. Wu, Y. Wang and H. Zeng, *Adv. Mater.*, 2019, **31**, 1900767.

8 Y. Zu, J. Xi, L. Li, J. Dai, S. Wang, F. Yun, B. Jiao, H. Dong, X. Hou and Z. Wu, *ACS Appl. Mater. Interfaces*, 2020, **12**, 2835–2841.

9 D. Luo, R. Su, W. Zhang, Q. Gong and R. Zhu, *Nat. Rev. Mater.*, 2020, **5**, 44–60.

10 T. Xuan, J. Huang, H. Liu, S. Lou, L. Cao, W. Gan, R.-S. Liu and J. Wang, *Chem. Mater.*, 2019, **31**, 1042–1047.

11 Q. Zeng, X. Zhang, C. Liu, T. Feng, Z. Chen, W. Zhang, W. Zheng, H. Zhang and B. Yang, *Sol. RRL*, 2019, **3**, 1800239.

12 H. Wang, S. Cao, B. Yang, H. Li, M. Wang, X. Hu, K. Sun and Z. Zang, *Sol. RRL*, 2020, **4**, 1900363.

13 C. Han, C. Li, Z. Zang, M. Wang, K. Sun, X. Tang and J. Du, *Photonics Res.*, 2017, **5**, 473–480.

14 C. Li, Z. Zang, C. Han, Z. Hu, X. Tang, J. Du, Y. Leng and K. Sun, *Nano Energy*, 2017, **40**, 195–202.

15 C. Li, Z. Zang, W. Chen, Z. Hu, X. Tang, W. Hu, K. Sun, X. Liu and W. Chen, *Opt. Express*, 2016, **24**, 15071–15078.

16 Y.-F. Li, S.-Y. Chou, P. Huang, C. Xiao, X. Liu, Y. Xie, F. Zhao, Y. Huang, J. Feng, H. Zhong, H.-B. Sun and Q. Pei, *Adv. Mater.*, 2019, **31**, 1807516.

17 X. Ling, S. Zhou, J. Yuan, J. Shi, Y. Qian, B. W. Larson, Q. Zhao, C. Qin, F. Li, G. Shi, C. Stewart, J. Hu, X. Zhang, J. M. Luther, S. Duhm and W. Ma, *Adv. Energy Mater.*, 2019, **9**, 1900721.

18 J. Yuan, C. Bi, S. Wang, R. Guo, T. Shen, L. Zhang and J. Tian, *Adv. Funct. Mater.*, 2019, **29**, 1906615.

19 K. Abdel-Latif, R. W. Epps, C. B. Kerr, C. M. Papa, F. N. Castellano and M. Abolhasani, *Adv. Funct. Mater.*, 2019, **29**, 1900712.

20 Q. Khan, A. Subramanian, G. Yu, K. Maaz, D. Li, R. U. R. Sagar, K. Chen, W. Lei, B. Shabbir and Y. Zhang, *Nanoscale*, 2019, **11**, 5021–5029.

21 J. Xue, R. Wang, L. Chen, S. Nuryyeva, T.-H. Han, T. Huang, S. Tan, J. Zhu, M. Wang, Z.-K. Wang, C. Zhang, J.-W. Lee and Y. Yang, *Adv. Mater.*, 2019, **31**, 1900111.

22 X. Zhang, C. Sun, Y. Zhang, H. Wu, C. Ji, Y. Chuai, P. Wang, S. Wen, C. Zhang and W. W. Yu, *J. Phys. Chem. Lett.*, 2016, **7**, 4602–4610.

23 M. Xiao, M. Hao, M. Lyu, E. G. Moore, C. Zhang, B. Luo, J. Hou, J. Lipton-Duffin and L. Wang, *Adv. Funct. Mater.*, 2019, **29**, 1905683.

24 X. Zhang, M. Lu, Y. Zhang, H. Wu, X. Shen, W. Zhang, W. Zheng, V. L. Colvin and W. W. Yu, *ACS Cent. Sci.*, 2018, **4**, 1352–1359.

25 S. Wang, C. Bi, J. Yuan, L. Zhang and J. Tian, *ACS Energy Lett.*, 2018, **3**, 245–251.

26 H. Wang, X. Zhang, Q. Wu, F. Cao, D. Yang, Y. Shang, Z. Ning, W. Zhang, W. Zheng, Y. Yan, S. V. Kershaw, L. Zhang, A. L. Rogach and X. Yang, *Nat. Commun.*, 2019, **10**, 665.

27 J. Wu, J. Tong, Y. Gao, A. Wang, T. Zhang, H. Tan, S. Nie and Z. Deng, *Angew. Chem., Int. Ed.*, 2020, DOI: 10.1002/anie.201911638.

28 D. Yan, T. Shi, Z. Zang, T. Zhou, Z. Liu, Z. Zhang, J. Du, Y. Leng and X. Tang, *Small*, 2019, **15**, 1901173.

29 H. Guan, S. Zhao, H. Wang, D. Yan, M. Wang and Z. Zang, *Nano Energy*, 2020, **67**, 104279.

30 X. Tang, W. Chen, Z. Liu, J. Du, Z. Yao, Y. Huang, C. Chen, Z. Yang, T. Shi, W. Hu, Z. Zang, Y. Chen and Y. Leng, *Small*, 2019, **15**, 1900484.

31 Q. Zeng, X. Zhang, X. Feng, S. Lu, Z. Chen, X. Yong, S. A. T. Redfern, H. Wei, H. Wang, H. Shen, W. Zhang, W. Zheng, H. Zhang, J. S. Tse and B. Yang, *Adv. Mater.*, 2018, **30**, 1705393.

32 R. P. Sabatini, G. Bappi, K. T. Bicanic, F. Fan, S. Hoogland, M. I. Saidaminov, L. K. Sagar, O. Voznyy and E. H. Sargent, *ACS Nano*, 2019, **13**, 8970–8976.

33 A. Fuhr, H. J. Yun, S. A. Crooker and V. I. Klimov, *ACS Nano*, 2020, **14**, 2212–2223.

34 Y. Kim, J. H. Chang, H. Choi, Y.-H. Kim, W. K. Bae and S. Jeong, *Chem. Sci.*, 2020, **11**, 913–922.

35 I. D. Skurlov, I. G. Korzhenevskii, A. S. Mudrak, A. Dubavik, S. A. Cherevkov, P. S. Parfenov, X. Zhang, A. V. Fedorov, A. P. Litvin and A. V. Baranov, *Materials*, 2019, **12**, 3219.

36 X. Li, Y. Wu, S. Zhang, B. Cai, Y. Gu, J. Song and H. Zeng, *Adv. Funct. Mater.*, 2016, **26**, 2435–2445.

37 F. Zhang, H. Zhong, C. Chen, X.-g. Wu, X. Hu, H. Huang, J. Han, B. Zou and Y. Dong, *ACS Nano*, 2015, **9**, 4533–4542.

38 S.-T. Ha, R. Su, J. Xing, Q. Zhang and Q. Xiong, *Chem. Sci.*, 2017, **8**, 2522–2536.

39 G. Grancini, V. D'Innocenzo, E. R. Dohner, N. Martino, A. R. Srimath Kandada, E. Mosconi, F. De Angelis, H. I. Karunadasa, E. T. Hoke and A. Petrozza, *Chem. Sci.*, 2015, **6**, 7305–7310.

40 H. Huang, B. Chen, Z. Wang, T. F. Hung, A. S. Susha, H. Zhong and A. L. Rogach, *Chem. Sci.*, 2016, **7**, 5699–5703.

41 M. Sygletou, M.-E. Kyriazi, A. G. Kanaras and E. Stratakis, *Chem. Sci.*, 2018, **9**, 8121–8126.

42 M. E. F. Bouduban, A. Burgos-Caminal, R. Ossola, J. Teuscher and J.-E. Moser, *Chem. Sci.*, 2017, **8**, 4371–4380.

43 S. Sun, D. Yuan, Y. Xu, A. Wang and Z. Deng, *ACS Nano*, 2016, **10**, 3648–3657.

44 A. Pan, B. He, X. Fan, Z. Liu, J. J. Urban, A. P. Alivisatos, L. He and Y. Liu, *ACS Nano*, 2016, **10**, 7943–7954.

45 A. Chakrabarty, S. Satija, U. Gangwar and S. Sapra, *Chem. Mater.*, 2020, **32**, 721–733.

46 Y. Li, H. Huang, Y. Xiong, A. F. Richter, S. V. Kershaw, J. Feldmann and A. L. Rogach, *ACS Nano*, 2019, **13**, 8237–8245.

47 J. Shamsi, Z. Dang, P. Bianchini, C. Canale, F. Di Stasio, R. Brescia, M. Prato and L. Manna, *J. Am. Chem. Soc.*, 2016, **138**, 7240–7243.

48 A. Dutta, R. K. Behera and N. Pradhan, *ACS Energy Lett.*, 2019, **4**, 926–932.

49 S. K. Balakrishnan and P. V. Kamat, *Chem. Mater.*, 2018, **30**, 74–78.

50 G. Li, H. Wang, Z. Zhu, Y. Chang, T. Zhang, Z. Song and Y. Jiang, *Chem. Commun.*, 2016, **52**, 11296–11299.

51 Z. Zhang, Y. Zhu, W. Wang, W. Zheng, R. Lin and F. Huang, *J. Mater. Chem. C*, 2018, **6**, 446–451.

52 P. Acharyya, P. Pal, P. K. Samanta, A. Sarkar, S. K. Pati and K. Biswas, *Nanoscale*, 2019, **11**, 4001–4007.

53 I. Dursun, M. De Bastiani, B. Turedi, B. Alamer, A. Shkurenko, J. Yin, A. M. El-Zohry, I. Gereige, A. AlSaggaf, O. F. Mohammed, M. Eddaoudi and O. M. Bakr, *ChemSusChem*, 2017, **10**, 3746–3749.

54 H. Yuan, E. Debroye, G. Caliandro, K. P. F. Janssen, J. van Loon, C. E. A. Kirschhock, J. A. Martens, J. Hofkens and M. B. J. Roeffaers, *ACS Omega*, 2016, **1**, 148–159.

55 B. Parida, J. Ryu, S. Yoon, S. Lee, Y. Seo, J. S. Cho and D.-W. Kang, *J. Mater. Chem. A*, 2019, **7**, 18488–18498.

56 L. Protesescu, S. Yakunin, M. I. Bodnarchuk, F. Krieg, R. Caputo, C. H. Hendon, R. X. Yang, A. Walsh and M. V. Kovalenko, *Nano Lett.*, 2015, **15**, 3692–3696.

57 A. Swarnkar, A. R. Marshall, E. M. Sanehira, B. D. Chernomordik, D. T. Moore, J. A. Christians, T. Chakrabarti and J. M. Luther, *Science*, 2016, **354**, 92–95.

58 X. Zhang, X. Bai, H. Wu, X. Zhang, C. Sun, Y. Zhang, W. Zhang, W. Zheng, W. W. Yu and A. L. Rogach, *Angew. Chem., Int. Ed.*, 2018, **57**, 3337–3342.

59 G. H. Ahmed, J. Yin, R. Bose, L. Sinatra, E. Alarousu, E. Yengel, N. M. AlYami, M. I. Saidaminov, Y. Zhang, M. N. Hedhili, O. M. Bakr, J.-L. Brédas and O. F. Mohammed, *Chem. Mater.*, 2017, **29**, 4393–4400.

60 H. Huang, J. Raith, S. V. Kershaw, S. Kalytchuk, O. Tomanec, L. Jing, A. S. Susha, R. Zboril and A. L. Rogach, *Nat. Commun.*, 2017, **8**, 996.

61 X. Zhang, Y. Zhang, L. Yan, C. Ji, H. Wu, Y. Wang, P. Wang, T. Zhang, Y. Wang, T. Cui, J. Zhao and W. W. Yu, *J. Mater. Chem. A*, 2015, **3**, 8501–8507.

62 M. Lu, X. Zhang, X. Bai, H. Wu, X. Shen, Y. Zhang, W. Zhang, W. Zheng, H. Song, W. W. Yu and A. L. Rogach, *ACS Energy Lett.*, 2018, **3**, 1571–1577.

63 Y. Wu, C. Wei, X. Li, Y. Li, S. Qiu, W. Shen, B. Cai, Z. Sun, D. Yang, Z. Deng and H. Zeng, *ACS Energy Lett.*, 2018, **3**, 2030–2037.

64 R. L. Z. Hoye, M.-L. Lai, M. Anaya, Y. Tong, K. Gałkowski, T. Doherty, W. Li, T. N. Huq, S. Mackowski, L. Polavarapu, J. Feldmann, J. L. MacManus-Driscoll, R. H. Friend, A. S. Urban and S. D. Stranks, *ACS Energy Lett.*, 2019, **4**, 1181–1188.

65 C. Zhang, Q. Wan, B. Wang, W. Zheng, M. Liu, Q. Zhang, L. Kong and L. Li, *J. Phys. Chem. B*, 2019, **123**, 26161–26169.